iScience

Article

Integrating gene-microbiome interactions and single-cell transcriptomics reveals therapeutic strategies for aortic aneurysm

Graphical abstract

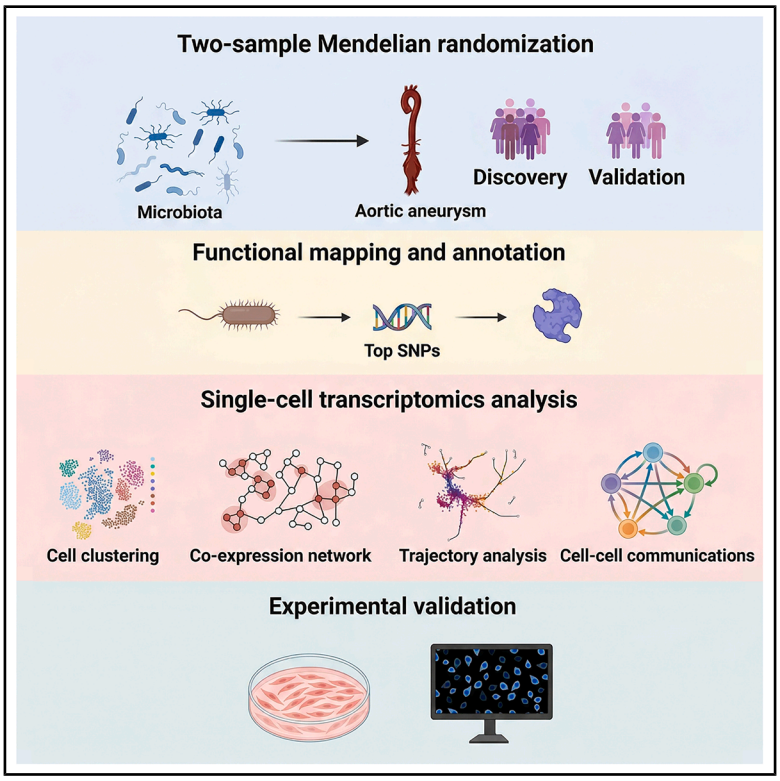

Highlights

- Mendelian randomization identifies *Intestinimonas* as protective against aortic aneurysm
- Genetic annotation pinpoints *CCDC3* as a causal gene in the gut-aorta axis
- *CCDC3* deficiency in VSMCs drives the CXCL12-CXCR4 axis in aortic aneurysm

Authors

Jiachen Liu, Weimin Han, Duan Wang, ..., Jiayin Guo, Yinghong Li, Xiangchen Dai

Correspondence

13302165917@163.com

In brief

cardiovascular medicine; omics

Liu et al., 2026, iScience *29*, 115939
June 19, 2026
https://doi.org/10.1016/j.isci.2026.115939

CellPress

iScience

CellPress
OPEN ACCESS

Article

Integrating gene-microbiome interactions and single-cell transcriptomics reveals therapeutic strategies for aortic aneurysm

Jiachen Liu,[1,2,4] Weimin Han,[3,4] Duan Wang,[1,2,4] Yierpani Aierken,[1,2] Zongwei Liu,[1,2] Jiaxin Wang,[1,2] Jiayin Guo,[1,2] Yinghong Li,[1,2] and Xiangchen Dai[1,2,5,*]

[1]Department of Vascular Surgery of Tianjin Medical University General Hospital, Tianjin, China
[2]Tianjin Key Laboratory of Precise Vascular Reconstruction and Organ Function Repair, Tianjin, China
[3]Beijing Anzhen Hospital, Capital Medical University, No. 2 Anzhen Road, Chaoyang District, Beijing 100029, China
[4]These authors contributed equally
[5]Lead contact
*Correspondence: 13302165917@163.com
https://doi.org/10.1016/j.isci.2026.115939

SUMMARY

Aortic aneurysm (AA) is a life-threatening vascular disorder lacking effective medical therapies. Gut microbiota contributes importantly to vascular homeostasis; yet, the underlying gene-microbiome interactions in AA remain unclear. Using two-sample Mendelian randomization, we identified and validated a protective causal effect of genus *Intestinimonas* abundance on AA risk. Genetic annotation pinpointed *CCDC3* as a causal gene in the gut-aorta axis. Integration of bulk and single-cell RNA sequencing revealed that *CCDC3* deficiency in vascular smooth muscle cells activates a pathogenic CXCL12-CXCR4 signaling axis, which recruits neutrophils and promotes neutrophil extracellular trap formation in aneurysmal tissue. These findings establish a mechanistic link between specific gut microbes, host genetics, and vascular inflammation at single-cell resolution, highlighting promising therapeutic targets for the treatment of aortic aneurysm.

INTRODUCTION

Aortic aneurysms (AAs) are characterized by progressive dilatation and weakening of the aortic wall. In recent years, the increased occurrence rate of AA has posed a significant threat to global health. The rupture-associated mortality rate is over 80%, which contributes to over 150,000 deaths worldwide each year.[1] Currently, the therapeutic options for AA are limited, with no effective methods except for the endovascular intervention or open surgery. However, surgical treatments are associated with high rupture and re-intervention rates.[2] Thus, it is urgent to develop effective therapeutic strategies to mitigate AA progression.

Gut microbiota, representing a diverse microbial community, plays a vital role in host physiology, including nutrient digestion, vitamin synthesis, and metabolite production.[3] Dysbiosis of gut microbiota has been demonstrated to be involved in AA progression.[4] However, previous studies focused on cross-sectional evidence,[5] limiting the ability to explain confounding factors. Gut microbiota abundance is often affected by lifestyle and environmental factors, including diet and medication.[6,7] As a classic epidemiological method, two-sample Mendelian randomization (MR) allows exploration of potential causality between exposures and diseases, which employs single-nucleotide polymorphisms (SNPs) as instruments to infer causality.[8] As a complex and heritable trait, the microbiome is influenced by the host genome, making the exploration of host gene-microbiome interactions a viable approach for discovering therapeutic targets.[9,10]

Single-cell transcriptomic analysis equipped researchers with a high-resolution tool to elucidate pathogenesis by leveraging discoveries from genome-wide association studies and analyzing the distinct features of cell composition, cell interactions, and differentiation trajectories.[11] However, most clinically utilized expression assays rely on the bulk transcriptome. Bulk RNA sequencing estimates the averaged properties of the entire tissue and offers valuable phenotypic information. Integrating bulk and single-cell transcriptomes is a promising approach for guiding the identification of pathogenic cell subsets and interpreting expression datasets from novel perspectives.[12]

In this study, we employed two-sample MR analyses to establish causal relationships between microbial abundance and AA. Furthermore, we provided the genetic interpretation of the significant associations and dissected underlying biological mechanisms using single-cell transcriptomic analysis. This integrative approach linked gene-microbiome interactions with cellular mechanisms, offering a foundation for precise intervention and targeted therapies.

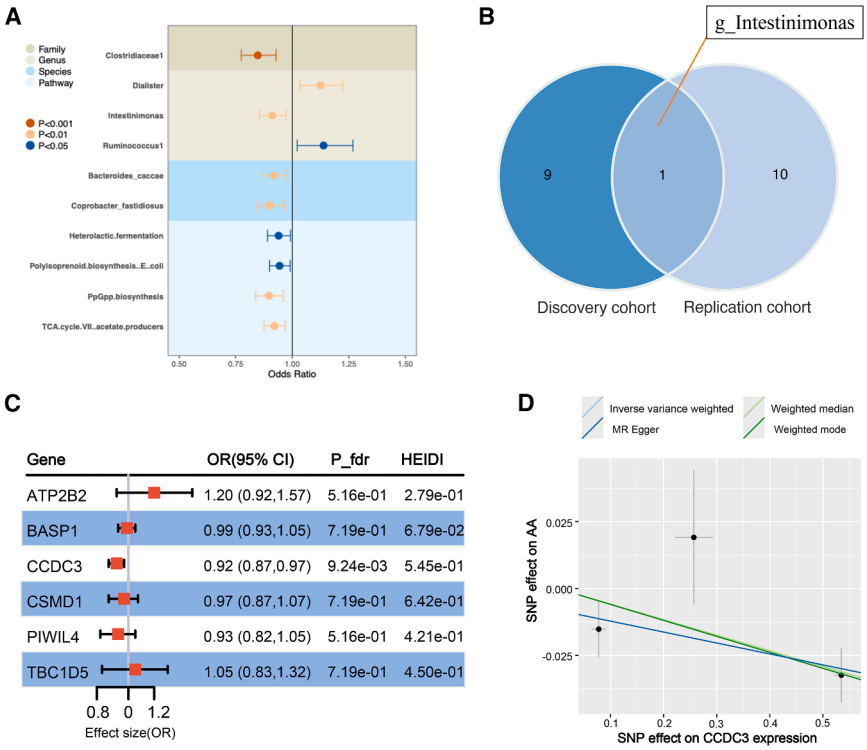

Figure 1. MR illustrating the host gene-microbiota causality in AA

(A) Forest plot revealing the causality between the abundance of gut microbiota taxa and AA.

(B) Venn plot showing the common gut microbiota correlated with AA between both discovery and validation cohorts.

(C) Forest plot revealing the causality between genetically predicted host gene expression and AA in summary-level MR analysis.

(D) Scatterplot showing the causality between genetically predicted *CCDC3* expression and AA in MR analysis. Estimates for MR analysis were obtained using the inverse variance weighted method. MR, Mendelian randomization.

RESULTS

Unraveling the gene-microbiome interactions in AA

The variance explained by each inverse variances (IVs) (R^2) and the strength of each IV (F statistics) were calculated (Table S3). Comprehensively considering the consistent directions of estimates in four methods, we discovered that ten microbial taxa exerted causal effects on AA in the discovery cohort (Figure 1). Among them, only the causality between the genus *Intestinimonas* and AA was significant in both datasets (OR = 0.91, p = 0.005, discovery cohort, Figure S2 and Table S4; OR = 0.72, p = 0.029, replication cohort; Table S7). Cochran's Q statistic indicated no heterogeneity in the causality (Table S5). MR-PRESSO and Egger analysis indicated the absence of intercepts and no horizontal pleiotropy (Table S6). The leave-one-out analyses revealed that no leverage points exerted significant influence (Figure S3). Reverse MR analysis suggested no reverse association between the genus *Intestinimonas* and AA (Table S8). We annotated the SNPs of genus *Intestinimonas* at a locus-wide significance level and identified nine protein-encoded genes (Table S9). We observed that mapped genes were more abundantly expressed in the aorta compared to other tissues (Figure S4). Notably, *CCDC3* exhibited the highest tissue specificity in the aorta (Figure S5). We further performed SMR analysis to estimate the causal effects of mapped host genes on AA. The results demonstrated that genetically predicted expression of *CCDC3* (OR = 0.92, p = 9.24e−03, Figure 1C) was negatively associated with AA, consistent with the MR analysis (IV weighted, OR = 0.94, p = 8.90e−03, Figure 1D).

Single-cell transcriptome identifies VSMC-specific loss of *CCDC3* in aneurysmal wall

To explore the cell-specific characteristics of *CCDC3* in the pathogenesis of AA, we constructed a single-cell transcriptomic profile for the aneurysmal and normal aorta. After data filtration and quality control, we divided the cell landscape into eleven distinct subpopulations. These clusters were annotated as endothelial cells (ECs), vascular smooth muscle cells (VSMCs), fibroblasts, mesenchymal stem cells, NK cells, B cells, T cells, myeloid cells, plasma cells, and mast cells (Figures 2A–2C). A greater proportion of fibroblasts and immune cells originated from aneurysmal tissue (Figure 2D). Notably, differential expression analysis revealed that *CCDC3* expression was specifically reduced in the VSMCs of aneurysmal tissue (Figure 2E and Table S10). The findings indicated that pathogenic *CCDC3* deficiency might be involved in AA progression.

CCDC3 deficiency is associated with activated chemotaxis signaling pathways

To investigate the underlying mechanism of *CCDC3* deficiency in AA pathogenesis, VSMCs were stratified into $CCDC3^{+}$VSMCs and $CCDC3^{-}$VSMCs. We performed WGCNA to identify unique expression patterns in $CCDC3^{-}$ VSMCs (Figure S6). Using the optimal soft-thresholding power, we identified five co-expression modules (Figure 2F), among which the brown module was specifically enriched in aneurysmal tissues (Figure 2G). The core interaction network of the brown module is depicted in Figure 2H. KEGG pathway enrichment analysis revealed that genes within the brown module were predominantly involved in the NF-κB signaling pathway, chemotaxis signaling pathway, and cytokine-cytokine receptor interactions (Figure 2I). Furthermore, *CXCL12*, *CXCL2*, and *CXCL8* were identified as shared genes in these pathways (Figure 2J), suggesting that *CCDC3* deficiency instigates a pro-chemotactic program to drive AA development.

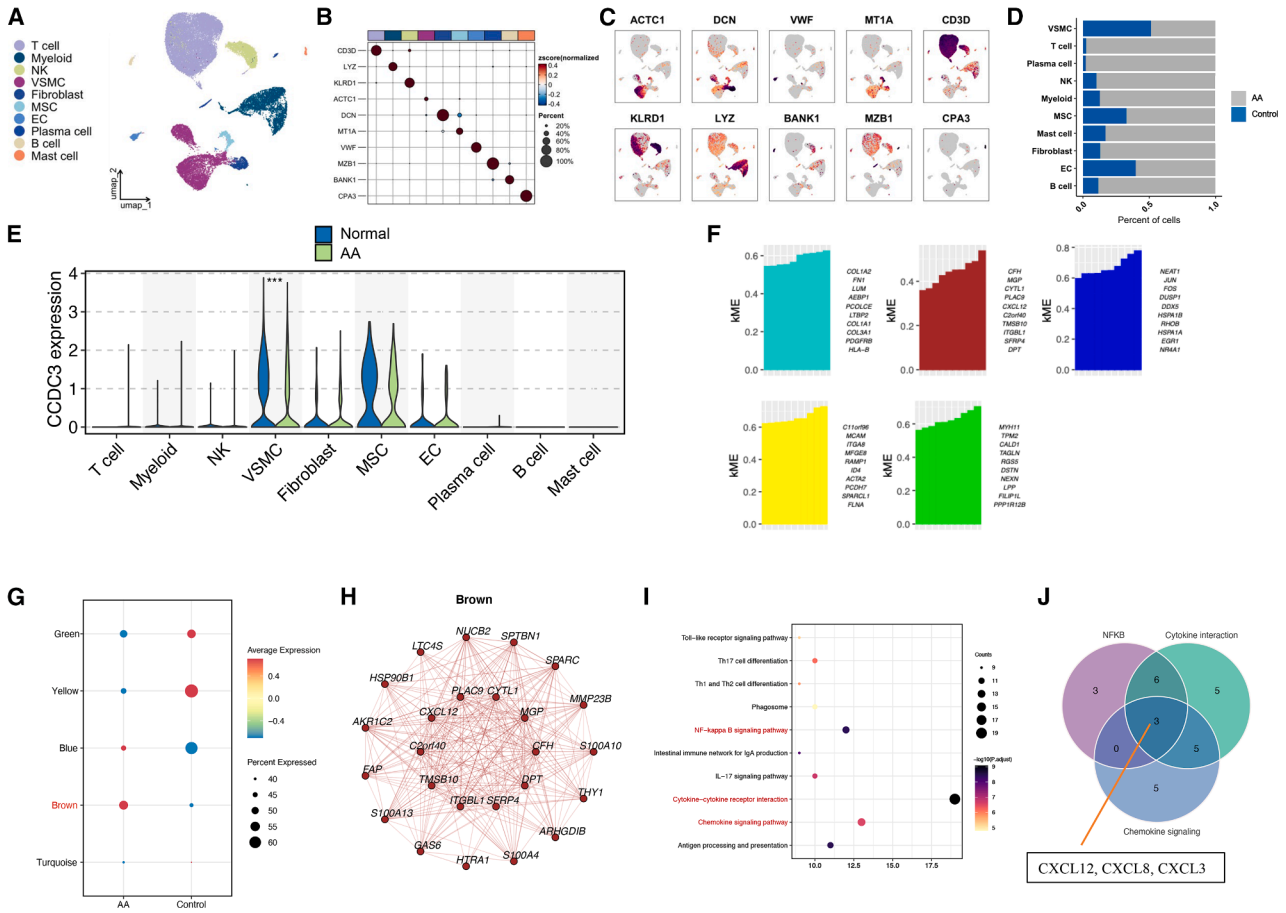

Figure 2. Single-cell transcriptomic landscape of aortic tissue

(A) UMAP plot illustrating the cell distribution profiles.

(B) Dot plot showing the top marker genes of major cell types.

(C) UMAP plots illustrating the expression of top cell markers for major cell types; the color indicates the expression value.

(D) Bar plots showing the proportion of tissue types in major cell types.

(E) Violin plot comparing the expression level of *CCDC3* in major cell types between AA and normal aorta.

(F) Ridge plots showing the five gene modules identified by co-expression analysis in CCDC3^{-}VSMCs.

(G) Dot plot showing the enrichment of major co-expression modules between AA and normal aorta.

(H) Co-expression network plot showing hub genes of the brown module.

(I) KEGG pathway enrichment analysis for genes in the brown module.

(J) Venn plot showing the shared genes in the top enrichment pathways of KEGG analysis. AA, aortic aneurysm. $^{*}p < 0.05$, $^{**}p < 0.01$, $^{***}p < 0.001$.

VSMC heterogeneity reveals distinct functional subpopulations

Given the pivotal roles of the heterogeneity and plasticity of VSMCs in AA progression, we classified VSMCs into seven distinct subpopulations according to their expression profiles: ACTC1^{+} VSMCs, IF6^{+}VSMCs, CEBPD^{+}VSMCs, NOV^{+}VSMCs, LTBP2^{+} VSMCs, CXC12^{+}VSMCs, and CCND1^{+}VSMCs (Figure 3A and Table S11). Among these, CEBPD^{+}VSMCs, NOV^{+}VSMCs, CXC12^{+}VSMCs, and CCND1^{+}VSMCs were enriched in aneurysmal tissues (Figures 3B and 3C). Based on previously reported classifications, VSMCs were classified into contractile VSMCs (cVSMCs), modulated VSMCs (mVSMCs), proliferating VSMCs (pVSMCs), and stress VSMCs (sVSMCs) according to their molecular signatures (Figure 3D). Specifically, IF6^{+}VSMCs and ACTC1^{+}VSMCs displayed contractile characteristics, evidenced by the expression of contraction-associated genes (*CARMN* and *ACTA2*). CCND1^{+}VSMCs were identified as proliferating VSMCs due to robust expression of the proliferation marker *CCND1*. NOV^{+}VSMCs, CXC12^{+}VSMCs, and LTBP2^{+}VSMCs were designated as mVSMCs, characterized by high expression levels of extracellular matrix-related genes (*MMP2*, *COL1A2*, and *VCAN*). CEBPD^{+}VSMCs were classified as sVSMCs owing to elevated expression of stress-associated genes (*MT1X* and *HSPB7*). To elucidate the potential function of these subpopulations, we performed signaling enrichment analysis for each cluster (Figure 3E). Notably, PROGENy analysis revealed significant enrichment of JAK/STAT, TNF-α, and TGF-β signaling pathways in CXC12^{+}VSMCs. Additionally, TGF-β and

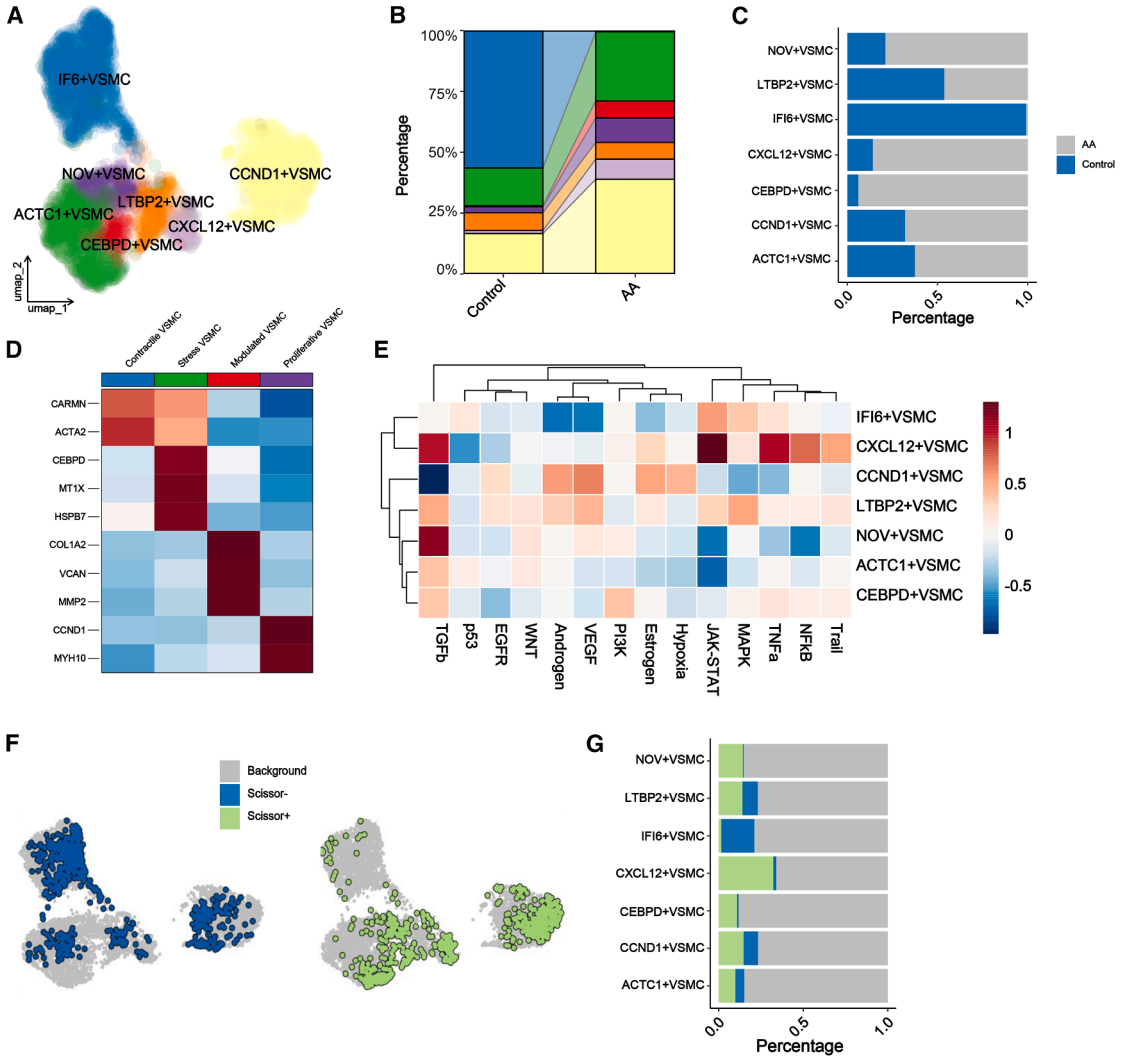

Figure 3. Heterogeneity and plasticity analysis for VSMCs

(A) UMAP plot showing the classification of VSMCs, with different colors representing different subtypes.

(B) Bar plots showing the proportion of the VSMC subtypes in AA and normal aorta.

(C) Bar plots showing the proportion of the tissue types in seven VSMC subtypes.

(D) Heatmap showing the top gene expression in the reclassified VSMC subtypes.

(E) Heatmap showing the key signaling pathways for seven VSMC subgroups calculated by the AUCell algorithm.

(F) UMAP showing the Scissor cells across VSMC subpopulations.

(G) Bar plots showing the proportion of the Scissor cells in seven VSMCs subtypes. AA, aortic aneurysm; VSMCs, vascular smooth muscle cells.

MAPK signaling were significantly enriched in NOV^{+} VSMCs and LTBP2^{+}VSMCs, respectively. Furthermore, CCND1^{+} VSMCs exhibited significant enrichment of the VEGF signaling pathway.

To directly link cell heterogeneity with AA, we applied Scissor to integrate single-cell profiles with phenotypic data from a reference dataset. Cells designated as scissor^{+} were inferred to associate with the AA phenotype, whereas scissor^{-}cells were associated with the normal aorta. This analysis robustly distinguished AA-related subpopulations in VSMCs (Figure 3F). Of 622 scissor^{+}cells, 443 (71.2%) originated from aneurysmal tissues, while 514 of 608 scissor^{-}cells (84.5%) were derived from healthy samples, indicating the high specificity of this approach. Notably, CXC12^{+}VSMCs, NOV^{+}VSMCs, and CEBPD^{+}VSMCs were markedly enriched in the scissor^{+}cells, whereas IF6^{+}VSMCs predominated in scissor^{-}cells (Figure 3G).

CCDC3 deficiency is associated with phenotypic switching into CXCL12^{+}VSMCs

To infer the dynamic transitions among VSMC subtypes, we established pseudotime trajectories and gained two principal lineages: cVSMCs occupied the progenitor state and bifurcated into either sVSMCs or mVSMCs (Figure S7). pVSMCs were localized to an independent trajectory branch.

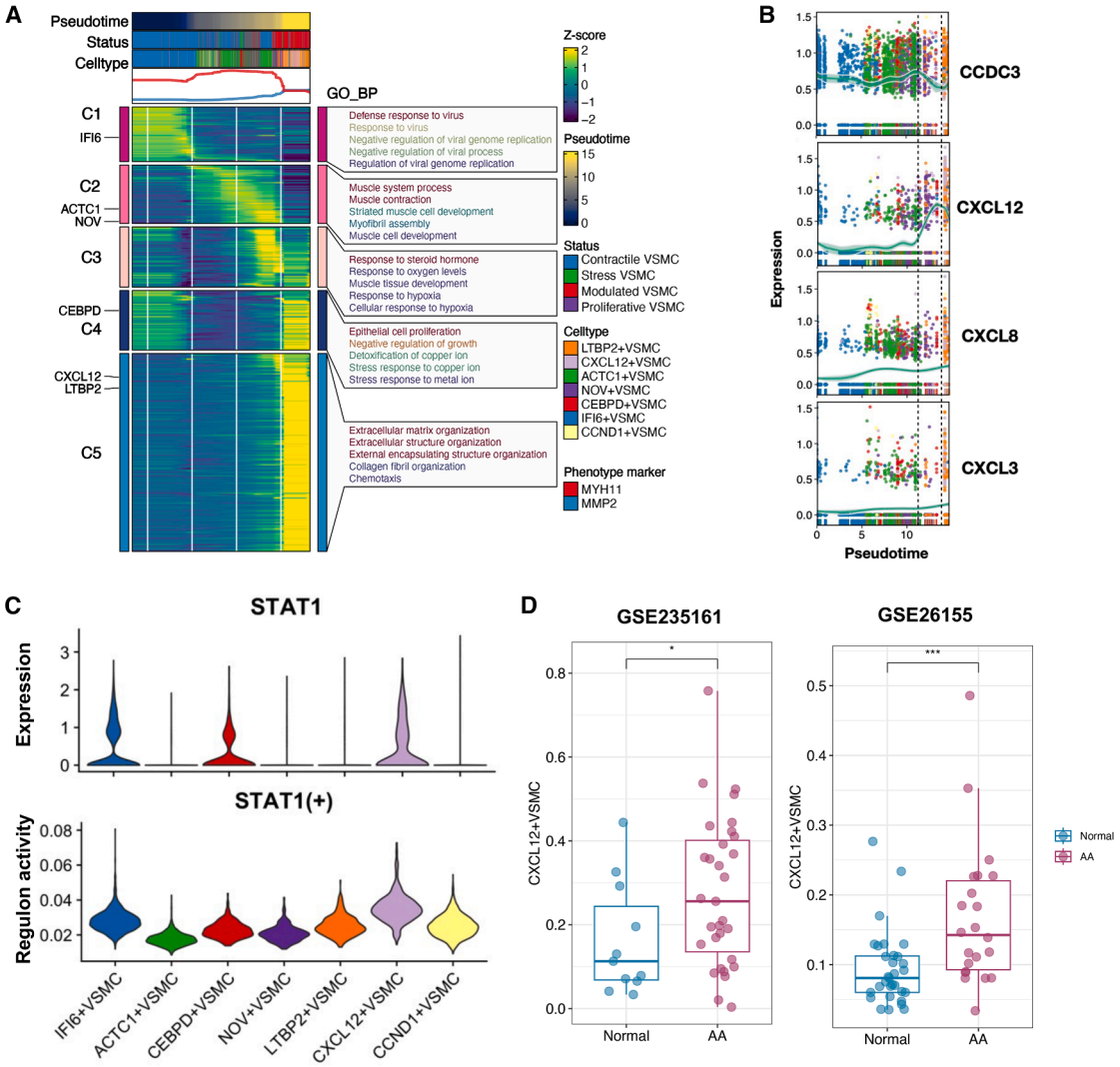

Figure 4. Trajectory analysis of VSMC subtypes

(A) Heatmap of signature genes in the trajectory branch (contractile VSMCs to modulated VSMCs) (left). Enrichment analysis showing the top five biological functions in each cluster (right).

(B) Pseudotime projections for expression in *CCDC3* deficiency-associated pathogenic genes (*CXCL12*, *CXCL8*, and *CXCL3*) and *CCDC3* in the trajectory branch (contractile VSMCs to modulated VSMCs).

(C) Violin plot showing the expression level and the regulon activity of the *STAT1* in VSMCs subpopulations.

(D) Comparing the enrichment of CXCL12^{+}VSMC between AA and normal aorta in microarray and bulk RNA-sequencing cohorts using deconvolution analysis. AA, aortic aneurysm; VSMCs, vascular smooth muscle cells. *$p < 0.05$, **$p < 0.01$, ***$p < 0.001$.

Gene expression dynamics along the trajectory revealed typical phenotypic shifts, with the contractile marker *MYH11* declining and the synthetic marker *MMP2* increasing over pseudotime (Figure 4A). Functional annotation indicated that genes enriched in the early trajectory (clusters 1–2) were associated with antiviral defense, muscle contraction, and developmental processes. Intermediate sVSMC states (clusters 3–4) were marked by signatures of hypoxia adaptation and metal-ion stress responses, whereas terminal mVSMCs (cluster 5) upregulated signatures linked to extracellular matrix remodeling and chemotaxis (Figure 4A).

Notably, a significant decrease in *CCDC3* expression was accompanied by pronounced upregulation of *CXCL12*, implying *CXCL12* as a downstream target of *CCDC3* deficiency (Figure 4B). We inferred that *STAT1* is a candidate transcriptional regulator of *CXCL12* through the pySCENIC method. The expression and regulon activity of *STAT1* were elevated in CXCL12^{+}VSMCs (Figure 4C). We assessed the proportion of VSMC subsets in two independent cohorts with the CIBERSORTx method and confirmed a higher percentage of CXCL12^{+}VSMCs in AA (Figure 4D). The findings elucidated that CCDC3 deficiency might facilitate CXCL12^{+}VSMCs formation via the JAK/STAT signaling pathway in AA.

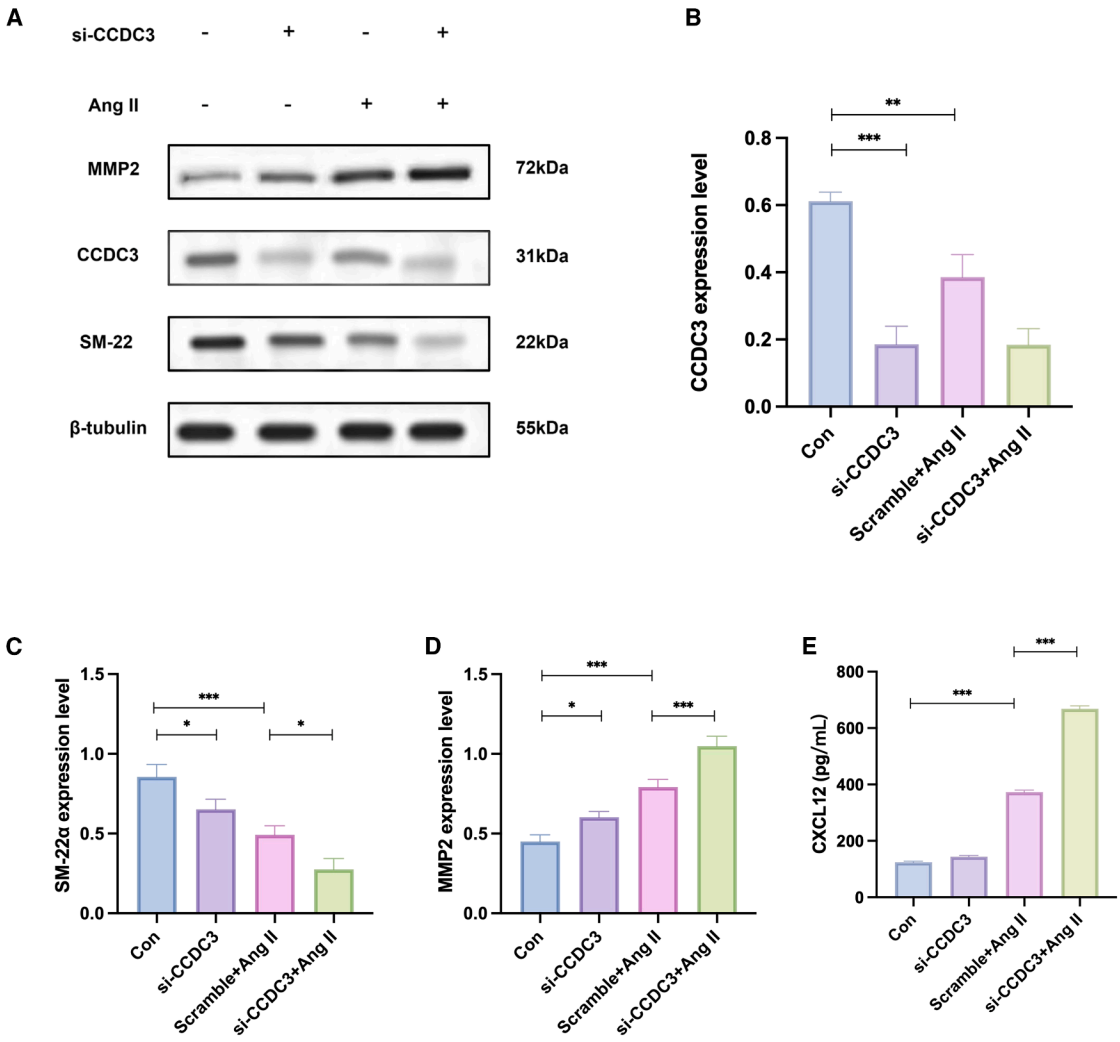

Figure 5. CCDC3 knockdown enhances angiotensin II-induced phenotypic switching of VSMCs and CXCL12 secretion *in vitro*

(A) Representative western blot images showing the protein expression of the contractile marker SM22α, the synthetic marker MMP2, and CCDC3 in four experimental groups: Control, si-*CCDC3*, Scramble+Ang II, and Ang II + si-*CCDC3* ($n = 3$).

(B–D) Quantification of CCDC3 (B), SM22α (C), and MMP2 (D) protein levels.

(E) CXCL12 concentrations in cell culture supernatants were quantified by ELISA across the four groups. Statistical comparisons among groups were performed using one-way ANOVA followed by Tukey's post hoc multiple comparison test. Data are expressed as mean ± SD.*$p < 0.05$, **$p < 0.01$, ***$p < 0.001$.

CCDC3 deficiency promotes Ang II-induced phenotypic switching of VSMCs toward a synthetic state

To validate the functional consequences of *CCDC3* deficiency in VSMCs, we performed *in vitro* experiments combining siRNA-mediated *CCDC3* knockdown (si-*CCDC3*) with Ang II stimulation (Figure 5A). Western blot analysis demonstrated that Ang II treatment significantly reduced the expression of *CCDC3* and the contractile marker SM22α, while si-*CCDC3* further augmented SM22α reduction (Figures 5B and 5C). Concordantly, the synthetic marker MMP2 was markedly upregulated upon Ang II stimulation, and its expression was further elevated by concurrent *CCDC3* knockdown (Figure 5D). At the secretory level, ELISA quantification revealed that Ang II-induced CXCL12 release was significantly potentiated in *CCDC3* knockdown VSMCs (Figure 5E). Collectively, these findings demonstrate that *CCDC3* deficiency promotes Ang II-induced VSMC phenotypic transition from a contractile to a synthetic state, accompanied by enhanced CXCL12 secretion.

VSMC-neutrophil interaction via the CXCL12/CXCR4 axis promotes NETs formation

To investigate cell communication in the aortic microenvironment, we applied the CellChat package to profile signaling interactions between VSMCs and other major cell types. Compared with normal tissues, aneurysmal samples exhibited enhanced crosstalk between VSMCs and myeloid cells (Figure 6A), implicating a VSMC-driven modulation of myeloid lineages in AA progression. We further identified 15 subtypes from the myeloid lineages based on specific marker genes: 11 macrophage clusters (SPP1^{+}Mph, CCL3L1^{+}Mph, F13A1^{+}Mph, MRC^{+}Mph, HLA-DRB5^{+}Mph,

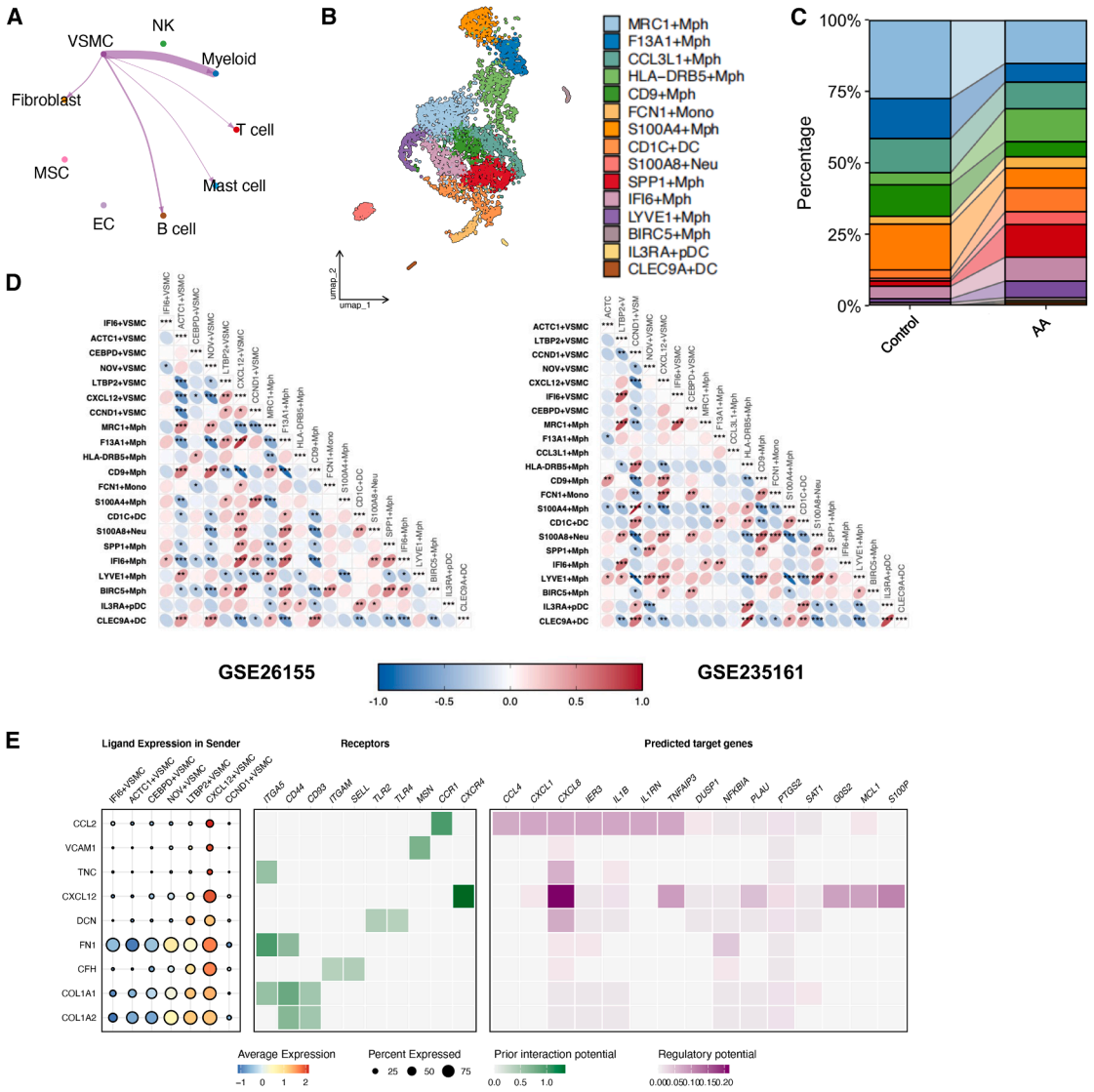

Figure 6. Characterization of pathogenic cell communications in AA

(A) Chord diagram showing the enhanced cell-cell interactions between VSMC and other major cell types in AA compared to the normal aorta. The line thickness indicates the increased strength.

(B) UMAP showing the heterogeneity of myeloid subsets in AA.

(C) Bar plots showing the proportion of the myeloid subtypes in AA and normal aorta.

(D) Dot plots showing the Spearman correlation for the pairwise infiltration of VSMC subtypes and myeloid subtypes in the microarray and bulk RNA-sequencing cohort. Dot size and color represent Spearman's correlation, and red (blue) dots indicate a positive (negative) relationship at different thresholds, $^{*}p < 0.05$, $^{**}p < 0.01$, $^{***}p < 0.001$.

(E) The ligand-receptor interaction between CXCL12^{+}VSMC and neutrophils according to NicheNet. The expression of top-ranked ligands between CXCL12^{+}VSMC and neutrophils in major VSMC subsets (left). The prior interaction potential of receptors for top-ranked ligands (middle). The regulatory potential of top-ranked ligands for predicted target genes (right).

CD9^{+}Mph, S100A4^{+}Mph, IFI6^{+}Mph, LYVE1^{+}Mph, and BIRC5^{+} Mph), one monocyte population (FCN1^{+}Mono), one neutrophil subtype (S100A8^{+}Neu), and three dendritic cell populations (CD1C^{+}DC, CLEC9A^{+}DC, and IL3RA^{+}pDC) (Figure 6B). Among these, SPP1^{+}Mph, HLA-DRB5^{+}Mph, LYVE1^{+}Mph, CD1C^{+}DCs, and S100A8^{+}neutrophils were significantly enriched in aneurysmal tissue (Figure 6C). We further assessed the myeloid cell infiltration and the relationships between VSMCs and myeloid subsets. The correlation analysis for two independent datasets suggested a shared positive association between CXCL12^{+}VSMCs and S100A8^{+}neutrophils (Figure 6D).

We applied the NicheNet algorithm to identify the key mechanisms in the interaction between CXCL12^{+}VSMCs and S100A8^{+}neutrophils. CXCL12^{+}VSMCs displayed elevated expression of *CCL2*, *TNC*, *VCAM1*, and *CXCL12*, which interact with their corresponding receptors CCR1, MSN, ITGA5, and

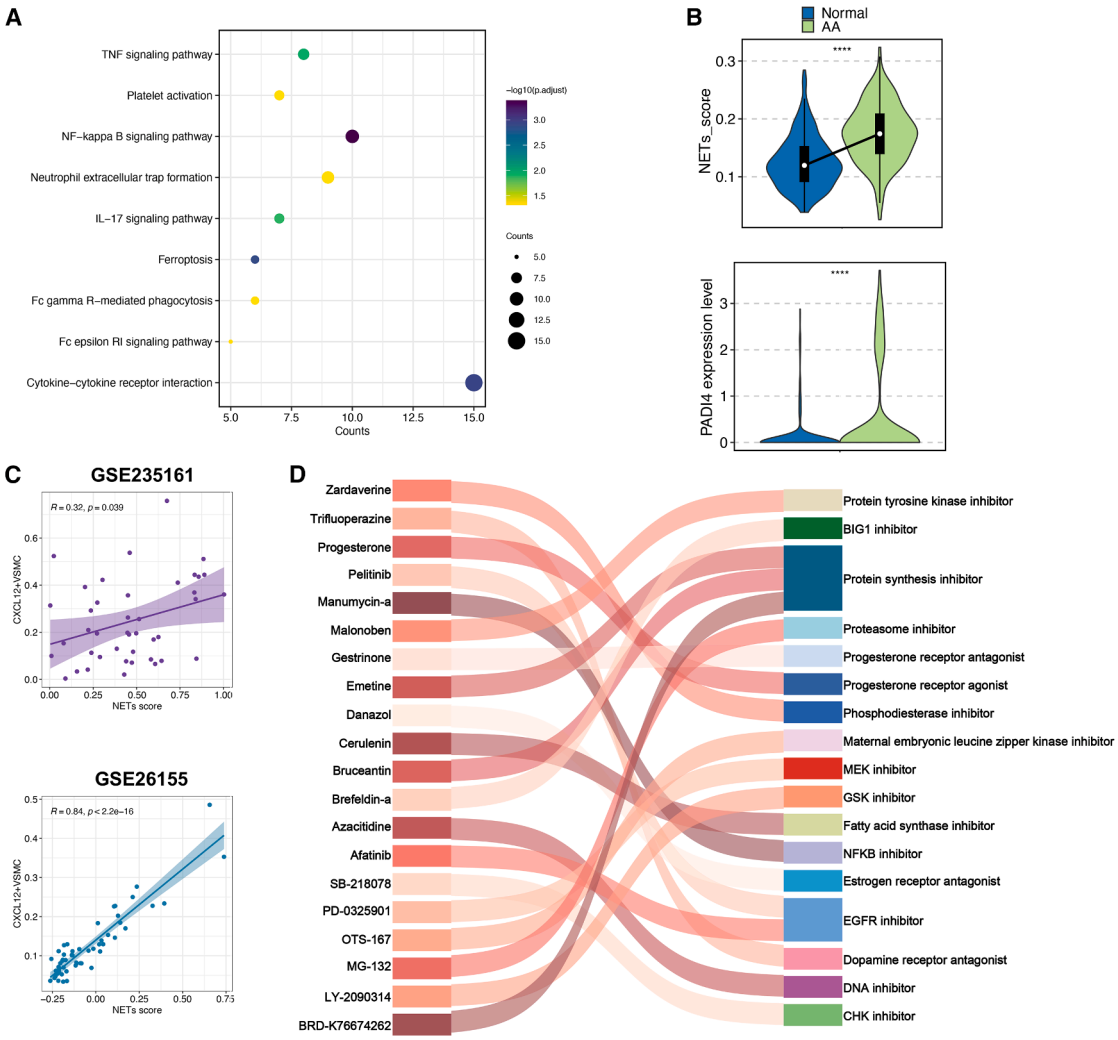

Figure 7. High infiltration of CXCL12^{+}VSMC and neutrophils was associated with NETs formation in AA

(A) KEGG pathway enrichment analysis for neutrophils showing increased NETs formation in AA.

(B) Violin plot showing the NETs activity and expression of NETs marker *PADI4*.

(C) Correlation scatterplots showing the relationships between CXCL12^{+}VSMC and neutrophils in microarray and bulk RNA-sequencing cohorts using deconvolution analysis.

(D) Sankey plots showing the top 20 small-molecule drugs for therapy.

*$p < 0.05$, **$p < 0.01$, ***$p < 0.001$.

CXCR4 on neutrophils (Figure 6E). Among these ligand-receptor pairs, the CXCL12-CXCR4 axis exhibited the strongest predicted interaction potential (Figure 6E). Consistently, *CXCR4* was highly expressed on neutrophils (Figure S8), suggesting that CXCL12^{+}VSMCs may recruit neutrophils through the CXCL12/CXCR4 axis. KEGG pathway analysis for neutrophils revealed significant enrichment of the neutrophil extracellular traps (NETs) formation in AA (Figure 7A). We further quantified NETs activity in neutrophils and observed an increase in NETs score within aneurysmal tissues, which was accompanied by elevated *PADI4* expression (Figure 7B). The NETs activity was further assessed in the microarray and RNA sequencing datasets and identified a significant positive association between CXCL12^{+}VSMCs and NETs score (Figure 7C). Collectively, the results uncovered a CXCL12^{+}VSMCs-neutrophil axis to foster NETs-dependent inflammation in AA.

Spatial transcriptomics and tissue validation

To investigate the spatial distribution of CXCL12^{+}VSMCs and S100A8^{+}neutrophils within the aortic microenvironment, we performed spatial transcriptomic analysis. Bayesian-enhanced spatial expression analysis revealed that regions of high *CXCL12* expression co-localized with areas of elevated *CXCR4*, *S100A8*, and *PADI4* expression in aneurysmal tissues (Figure 8A). Conversely, regions characterized by high *CCDC3* expression in the normal aortic wall exhibited markedly lower expression of *CXCL12*, *CXCR4*, *S100A8*, and *PADI4*. Furthermore, the signature scores of CXCL12^{+}VSMCs and

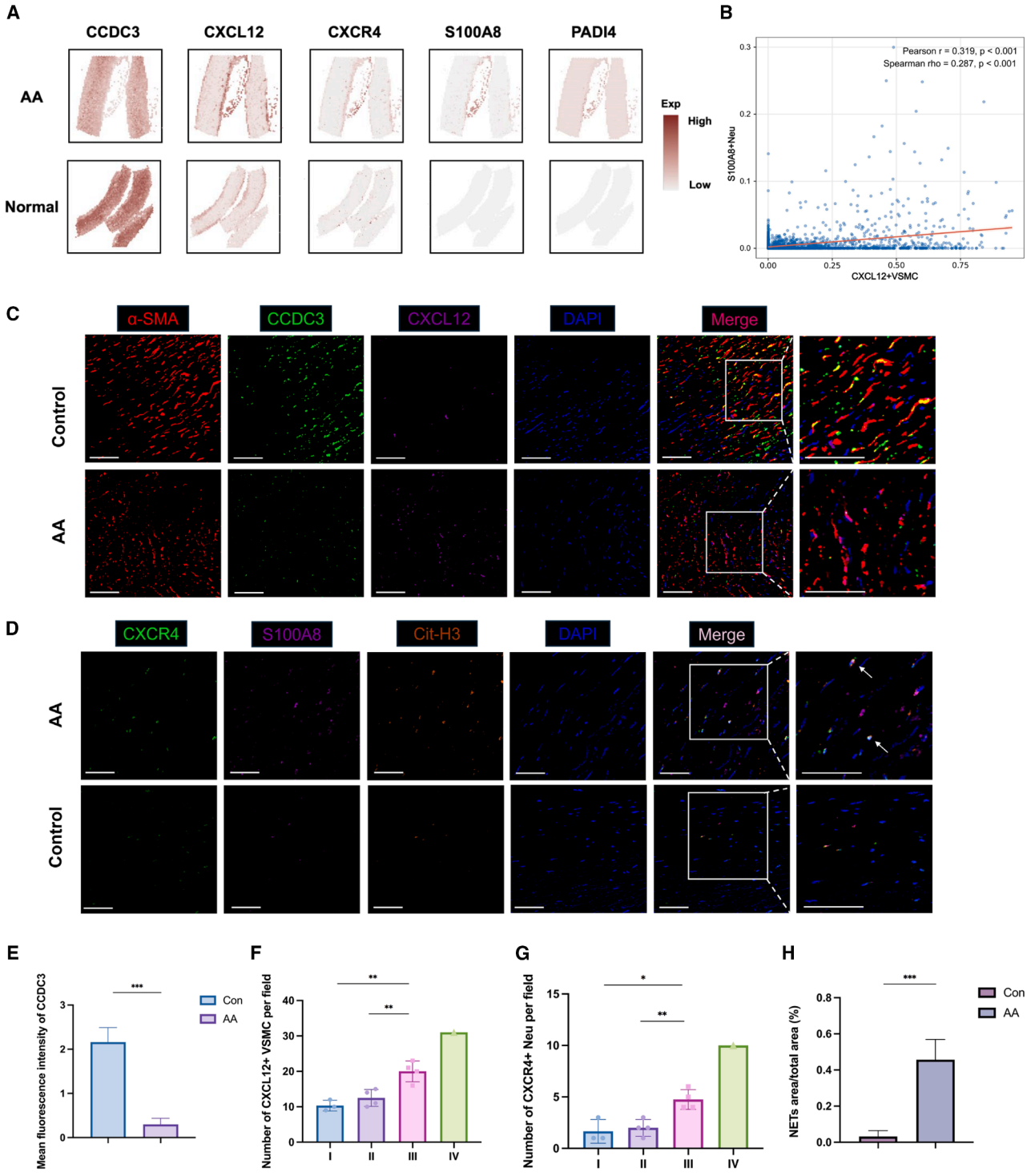

Figure 8. Spatial and immunofluorescence characterization of the CCDC3-CXCL12-CXCR4-NETs axis in human aortic tissues

(A) Bayesian-enhanced spatial feature plots displaying the expression of *CCDC3*, *CXCL12*, *CXCR4*, *S100A8*, and *PADI4* in representative aneurysmal and non-aneurysmal aortic tissues.

(B) Correlation analysis between CXCL12^{+}VSMCs and S100A8^{+}neutrophils in aneurysmal tissues.

(C) Representative multiplex immunofluorescence (mIF) images of aneurysmal and non-aneurysmal tissues co-stained for α-SMA (red), CCDC3 (green), CXCL12 (purple), and DAPI (blue); individual and merged channels are shown.

(legend continued on next page)

S100A8$^+$neutrophils were positively correlated across spatial spots (Figure 8B), collectively supporting the spatial co-enrichment of these two populations.

Multiplex immunofluorescence (mIF) staining demonstrated a significant reduction in *CCDC3* expression within aneurysmal lesions relative to non-aneurysmal controls (Figures 8C and 8E). To further characterize the CXCL12-CXCR4-NETs axis in human aortic tissues, we quantified the abundance of CXCL12$^+$VSMCs and CXCR4$^+$neutrophils across tissue groups. Both populations were significantly enriched in aneurysmal lesions compared with non-aneurysmal controls (Figure 8D), and their accumulation was positively correlated with the severity of elastin degradation (Figures 8F and 8G). NETs deposition was assessed by citrullinated histone H3 (CitH3) immunostaining. In aneurysmal lesions, CitH3 signal co-localized with CXCR4 and S100A8 positive regions. By contrast, non-aneurysmal tissues exhibited markedly attenuated signals for CXCR4, S100A8, and CitH3 (Figure 8H).

CMap identifies potential therapeutic drugs targeting *CCDC3* deficiency

To identify underlying therapeutic drugs targeting *CCDC3* deficiency-induced inflammation in AA, we utilized drug-response signatures in the CMap database. The top 20 small-molecule compounds negatively correlated with the brown module gene signature were identified (Figure 7D), including NF-κB inhibitors, MEK inhibitors, and proteasome inhibitors. Among these candidates, two compounds—mirdametinib and trifluoperazine—emerged as promising agents with potential therapeutic effects on CCDC3$^-$VSMCs and NETs formation. Mirdametinib, a selective MEK inhibitor, demonstrated therapeutic potential in AA by suppressing inflammatory cytokine expression and mitigating hypoxia-induced phenotypic switching of VSMCs.[13] In addition, MEK inhibition effectively attenuates NETosis by targeting the MEK1/2 kinase pathway.[14] Trifluoperazine, identified as the most promising calmodulin inhibitor, has established therapeutic relevance in conditions such as calcium-overloaded myocardium and pulmonary arterial hypertension.[15,16] Mechanistically, trifluoperazine interferes with calmodulin-dependent calcium signaling, thereby inhibiting NETosis through the reduction of reactive oxygen species production and subsequent inflammatory cascades critical for NETs formation.[17]

DISCUSSION

As an emerging concept, gut-aorta axis offers insights into therapeutic avenues for aortic diseases.[18] An imbalance in gut microbiota composition is increasingly linked to various cardiovascular diseases, including heart failure, hypertension, and atherosclerosis.[19,20] In our study, we obtained several key findings by integrating evidence from the microbiome and single-cell transcriptome. First, we established a robust causality between the genus *Intestinimonas* and AA progression. Second, we demonstrated *CCDC3* as a causal host gene in the modulation of AA through the gut-aorta axis. Finally, we revealed a possible mechanism that CCDC3 deficiency in VSMCs enhances the intercellular CXCL12/CXCR4 crosstalk, thus promoting NETs formation in AA.

Our findings suggested a protective effect of increased abundance of *Intestinimonas* on AA. *Intestinimonas*, particularly the species *Intestinimonas butyriciproducens*, exert a protective effect on cardiovascular disease risk by converting dietary compounds into short-chain fatty acids like butyrate. These metabolites improve insulin sensitivity and reduce metabolic inflammation, benefiting metabolic health and lowering risk for heart failure and atherosclerosis.[21–23] Consistent with this, butyrate produced by *Roseburia intestinalis* could inhibit aberrant phenotypic switching of VSMCs and NETs formation, thus significantly suppressing AA progression.[18]

Genetic interpretation revealed an enrichment of microbiome-related gene expression in the aorta, supporting the gut-aorta axis in AA. Furthermore, we identified *CCDC3* as a host gene linking AA with microbiota abundance. As a secretory protein, *CCDC3* is abundantly expressed in the artery and adipose tissues. In recent years, it has been known for diverse roles, including regulating lipid metabolism, inhibiting atherosclerosis, and suppressing pro-inflammatory responses in ECs.[24,25] *CCDC3* overexpression could inhibit TNF-α/NF-κB signaling-induced inflammation.[26] Additionally, *CCDC3* was significantly downregulated in human atherosclerotic lesions and exhibited a progressive decrease with advancing severity.[27] *CCDC80*, another member of the coiled-coil domain-containing protein family, plays a protective role against aortic dissection progression and rupture.[28] CCDC80 interacts with JAK2 to suppress VSMC phenotype switching, and its deficiency activates the JAK/STAT3 signaling pathway.[28] *CCDC80* deficiency is also associated with increased elastin fragmentation and collagen deposition in the aortic wall.[28] However, the specific role of *CCDC3* in AA remained unclear. We found that *CCDC3* is abundant in cVSMCs and declines in synthetic VSMCs. *CCDC3* deficiency is associated with activated JAK/STAT and TNF-α/NF-κB signaling pathways in AA.

As a primary component of the aorta, VSMCs display remarkable plasticity in response to stimuli, which is essential to preserve vascular integrity.[29–31] However, persistent VSMCs phenotypic switching induces poor tissue remodeling and facilitates AA development.[31,32] Integrating external phenotypic information and trajectory analysis, we identified CXCL12$^+$VSMC as a pathogenic subset associated with *CCDC3* deficiency, further emphasizing the crucial role of CXCL12-CXCR4 chemotactic axis in aneurysm progression. *CXCL12*, a chemokine,

(D) Representative mIF images co-stained for DAPI (blue), CXCR4 (green), S100A8 (purple), and citrullinated histone H3 (CitH3, orange); individual and merged channels are shown.
(E) Mean fluorescence intensity of CCDC3 in VSMCs between aneurysmal and non-aneurysmal tissues (n = 4).
(F and G) Correlation between elastin degradation grade and the abundance of CXCL12$^+$VSMCs (F) and CXCR4$^+$ neutrophils (G) in aneurysmal tissues (n = 4, three fields per sample).
(H) Quantification of NETs deposition, expressed as CitH3$^+$ area normalized to total tissue area (%), in aneurysmal versus non-aneurysmal tissues (n = 4). Scale bars, 50 μm. Data are presented as mean ± SD. Statistical significance was assessed using a two-sided Mann-Whitney U test. *p < 0.05; **p < 0.01; ***p < 0.001.

mobilizes leukocytes and other immune cells from bone marrow into circulating blood and subsequently into aortic tissues by interacting with CXCR4 at the early AA state.[33] As a synthetic VSMC, CXCL12^{+}VSMCs might recruit neutrophils via CXCL12/CXCR4 axis in aortic dissection.[34] Neutrophil infiltration could generate diverse inflammatory signals that enhance leukocyte recruitment and sustain inflammation, ultimately leading to tissue destruction.[35,36] NETs, consisting of extracellular webs of chromatin, DNA, and proteins, contribute to the inflammation and structural degradation of the aortic wall, leading to the development and growth of the aneurysm.[37,38] Elevated levels of NETs and their components are observed in AAA patients and animal models.[39] Moreover, NETs level in plasma could predict adverse aortic events after endovascular therapy.[40] Neutrophils with high *CXCR4* expression have a greater capacity to release NETs and show enhanced pro-inflammatory functions compared to low *CXCR4* expression neutrophils.[41] CXCR4 signaling inhibitor not only alleviates the immune infiltration of the aortic wall but also suppresses the phenotypic switching of cVSMCs into macrophage-like VSMCs.[42]

The findings highlight the potential therapeutic implications of enhancing the abundance of *Intestinimonas* to alleviate AA. Additionally, targeting the expression of *CCDC3* emerges as a promising strategy for mitigating AA. We further focused on the pathophysiological roles of *CCDC3* and elucidate potential molecular mechanisms at the single-cell level, facilitating the development of therapeutic interventions.

Limitations of the study

A notable strength of this study lies in discovering gene-microbiome interactions and unraveling the potential molecular mechanisms at single-cell resolution. However, several limitations should be acknowledged. First, recognizing the importance of having an adequate number of instrument variables for a robust analysis, a broader threshold was considered. Second, the population predominantly comprised individuals of European ancestry, potentially constraining the generalizability. Finally, although our integrative analysis uncovers causal relationships and underlying mechanisms of gene-microbiome interactions, these findings need to be validated by further experiments.

RESOURCE AVAILABILITY

Lead contact

Requests for further information should be directed to and will be fulfilled by the lead contact, Xiangchen Dai (13302165917@163.com).

Materials availability

This study did not generate new unique reagents.

Data and code availability

Data generated or analyzed during this study are publicly available. Publicly available datasets with accession numbers are comprehensively documented in the key resources table. The publicly available code and software are listed in the key resources table. Any additional information required to reanalyze the data reported in this study is available from the lead contact upon request.

ACKNOWLEDGMENTS

We thank the participants from the GWAS cohort included in this study, together with MiBioGen, UK Biobank, AAAGen, and the Dutch Microbiome Project for their valuable contributions. This study is supported by the National Natural Science Foundation of China (82241207 and 82070489).

AUTHOR CONTRIBUTIONS

Conceptualization, J.L., W.H., and D.W.; methodology, J.L., Z.L., and J.G.; software, formal analysis, and investigation, J.L., Y.A., and J.W.; writing – original draft, J.L.; writing – review and editing, Y.L., Y.A., and X.D.; funding acquisition, X.D.; supervision, W.H. and X.D.

DECLARATION OF INTERESTS

The authors declare no conflict of interest.

STAR★METHODS

Detailed methods are provided in the online version of this paper and include the following:

- KEY RESOURCES TABLE
- EXPERIMENTAL MODEL AND STUDY PARTICIPANT DETAILS
  - Human aortic tissue samples
  - Cell culture
- METHOD DETAILS
  - Cell treatment and transfection
  - Western blotting
  - ELISA
  - Histological and immunofluorescence staining
  - Data sources
  - MR design
  - Genetic annotation and tissue enrichment
  - Single-cell transcriptomics analysis
  - Deconvolution analysis for RNA-seq
  - Functional pathway and gene set enrichment analysis
  - Trajectory analysis
  - Cell-cell communications analysis
  - Spatial transcriptomics analysis
  - Drug sensitivity analysis
- QUANTIFICATION AND STATISTICAL ANALYSIS

SUPPLEMENTAL INFORMATION

Supplemental information can be found online at https://doi.org/10.1016/j.isci.2026.115939.

Received: October 14, 2025
Revised: April 4, 2026
Accepted: April 27, 2026
Published: April 30, 2026

REFERENCES

1. McClure, R.S., Brogly, S.B., Lajkosz, K., McClintock, C., Payne, D., Smith, H.N., and Johnson, A.P. (2020). Economic burden and healthcare resource use for thoracic aortic dissections and thoracic aortic aneurysms—A population-based cost-of-illness analysis. J. Am. Heart Assoc. *9*, e014981. https://doi.org/10.1161/JAHA.119.014981.
2. Lederle, F.A., Kyriakides, T.C., Stroupe, K.T., Freischlag, J.A., Padberg, F.T., Matsumura, J.S., Huo, Z., and Johnson, G.R. (2019). Open versus endovascular repair of abdominal aortic aneurysm. N. Engl. J. Med. *380*, 2126–2135. https://doi.org/10.1056/NEJMoa1715955.

3. Witkowski, M., Weeks, T.L., and Hazen, S.L. (2020). Gut microbiota and cardiovascular disease. Circ. Res. *127*, 553–570. https://doi.org/10.1161/CIRCRESAHA.120.316242.

4. Xie, J., Lu, W., Zhong, L., Hu, Y., Li, Q., Ding, R., Zhong, Z., Liu, Z., Xiao, H., and Xie, D. (2020). Alterations in gut microbiota of abdominal aortic aneurysm mice. BMC Cardiovasc. Disord. *20*, 1–7. https://doi.org/10.1186/s12872-020-01728-4.

5. Inoue, E., Ogawa, T., Tanaka, N., Nishimura, H., Hayashi, A., Ogawa, T., Xu, J.-Z., Kudo, S., Nishimura, Y., Ogawa, T., et al. (2023). Impact of Bifidobacterium adolescentis in patients with abdominal aortic aneurysm: a cross-sectional study. Biosci. Microbiota Food Health *42*, 261–268. https://doi.org/10.12938/bmfh.2022-055.

6. David, L., Maurice, C., Carmody, R., Gootenberg, D., Button, J., Wolfe, B., Ling, A., Devlin, A., Varma, Y., Fischbach, M., et al. (2014). Diet rapidly and reproducibly alters the human gut microbiome. Nature *505*, 559–563. https://doi.org/10.1038/nature12820.

7. Maier, L., Pruteanu, M., Kuhn, M., Zeller, G., Telzerow, A., Anderson, E.E., Brochado, A.R., Fernandez, K.C., Dose, H., Mori, H., et al. (2018). Extensive impact of non-antibiotic drugs on human gut bacteria. Nature *555*, 623–628. https://doi.org/10.1038/nature25979.

8. Lawlor, D., Harbord, R., Sterne, J., Timpson, N., and Davey Smith, G. (2008). Mendelian randomization: using genes as instruments for making causal inferences in epidemiology. Stat. Med. *27*, 1133–1163. https://doi.org/10.1002/sim.3034.

9. Hughes, D., Bacigalupe, R., Wang, J., Rühlemann, M., Tito, R., Falony, G., Joossens, M., Vieira-Silva, S., Henckaerts, L., Rymenans, L., et al. (2020). Genome-wide associations of human gut microbiome variation and implications for causal inference analyses. Nat. Microbiol. *5*, 1079–1087. https://doi.org/10.1038/s41564-020-0743-8.

10. Goodrich, J.K., Waters, J.L., Poole, A.C., Sutter, J.L., Koren, O., Blekhman, R., Beaumont, M., Van Treuren, W., Knight, R., Bell, J.T., et al. (2014). Human genetics shape the gut microbiome. Cell *159*, 789–799. https://doi.org/10.1016/j.cell.2014.09.053.

11. Yofe, I., Dahan, R., and Amit, I. (2020). Single-cell genomic approaches for developing the next generation of immunotherapies. Nat. Med. *26*, 171–177. https://doi.org/10.1038/s41591-019-0736-4.

12. Sun, D., Guan, X., Moran, A.E., Wu, L.-Y., Qian, D.Z., Schedin, P., Dai, M.-S., Danilov, A.V., Alumkal, J.J., and Adey, A.C. (2022). Identifying phenotype-associated subpopulations by integrating bulk and single-cell sequencing data. Nat. Biotechnol. *40*, 527–538. https://doi.org/10.1038/s41587-021-01091-3.

13. Zhang, W., Guo, Z., Li, L., Shi, Z., and Zhu, T. (2022). Hypoxia promotes human umbilical vein smooth muscle cell phenotypic switching via the ERK 1/2/c-fos/NF-κB signaling pathway. Ann. Vasc. Surg. *84*, 371–380. https://doi.org/10.1016/j.avsg.2022.03.038.

14. Tatsiy, O., and McDonald, P. (2018). Physiological stimuli induce PAD4-dependent, ROS-independent NETosis, with early and late events controlled by discrete signaling pathways. Front. Immunol. *9*, 2036. https://doi.org/10.3389/fimmu.2018.02036.

15. Grobs, Y., Awada, C., Lemay, S.-E., Romanet, C., Bourgeois, A., Toro, V., Nadeau, V., Shimauchi, K., Orcholski, M., Breuils-Bonnet, S., et al. (2021). Preclinical investigation of trifluoperazine as a novel therapeutic agent for the treatment of pulmonary arterial hypertension. Int. J. Mol. Sci. *22*, 2919. https://doi.org/10.3390/ijms22062919.

16. Hong, D., Son, Y., Li, H., Jung, I., Park, Y.-M., Jung, W.-K., Kim, H., Choi, I.-W., and Park, W. (2014). The calmodulin inhibitor and antipsychotic drug trifluoperazine inhibits voltage-dependent K+ channels in rabbit coronary arterial smooth muscle cells. Biochem. Biophys. Res. Commun. *443*, 321–325. https://doi.org/10.1016/j.bbrc.2013.11.115.

17. Yalcinkaya, M., Liu, W., Xiao, T., Abramowicz, S., Wang, R., Wang, N., Westerterp, M., and Tall, A. (2024). Cholesterol trafficking to the ER leads to the activation of CaMKII/JNK/NLRP3 and promotes atherosclerosis. J. Lipid Res. *65*, 100534. https://doi.org/10.1016/j.jlr.2024.100534.

18. Tian, Z., Zhang, Y., Zheng, Z., Zhang, M., Zhang, T., Jin, J., Zhang, X., Yao, G., Kong, D., Zhang, C., et al. (2022). Gut microbiome dysbiosis contributes to abdominal aortic aneurysm by promoting neutrophil extracellular trap formation. Cell Host Microbe *30*, 1450–1463.e8. https://doi.org/10.1016/j.chom.2022.09.004.

19. Muttiah, B., and Hanafiah, A. (2025). Gut microbiota and cardiovascular diseases: unraveling the role of dysbiosis and microbial metabolites. Int. J. Mol. Sci. *26*, 4264. https://doi.org/10.3390/ijms26094264.

20. Luqman, A., Hassan, A., Ullah, M., Naseem, S., Ullah, M., Zhang, L., Din, A.U., Ullah, K., Ahmad, W., and Wang, G. (2024). Role of the intestinal microbiome and its therapeutic intervention in cardiovascular disorder. Front. Immunol. *15*, 1321395. https://doi.org/10.3389/fimmu.2024.1321395.

21. Le Sayec, M., Xu, Y., Laiola, M., Gallego, F., Katsikioti, D., Durbidge, C., Kivisild, U., Armes, S., Lecomte, M., Fança-Berthon, P., et al. (2022). The effects of Aronia berry (poly)phenol supplementation on arterial function and the gut microbiome in middle aged men and women: results from a randomized controlled trial. Clin. Nutr. *41*, 2549–2561. https://doi.org/10.1016/j.clnu.2022.08.024.

22. Li, Q., Zhang, X., Du, Y., Liu, X., Chen, G., Xiang, P., Wu, H., Liu, C., and Wang, D. (2022). Brussels chicory stabilizes unstable atherosclerotic plaques and reshapes the gut microbiota in Apoe-/- mice. J. Nutr. *152*, 2209–2217. https://doi.org/10.1093/jn/nxac103.

23. Rampanelli, E., Romp, N., Troise, A.D., Ananthasabesan, J., Wu, H., Gül, I.S., De Pascale, S., Scaloni, A., Bäckhed, F., and Fogliano, V. (2025). Gut bacterium Intestinimonas butyriciproducens improves host metabolic health: evidence from cohort and animal intervention studies. Microbiome *13*, 15. https://doi.org/10.1186/s40168-024-02002-9.

24. Kobayashi, S., Fukuhara, A., Taguchi, T., Matsuda, M., Tochino, Y., Otsuki, M., and Shimomura, I. (2010). Identification of a new secretory factor, CCDC3/Favine, in adipocytes and endothelial cells. Biochem. Biophys. Res. Commun. *392*, 29–35. https://doi.org/10.1016/j.bbrc.2009.12.142.

25. Omari, S., Lee, H., Wang, J., Zeng, S.X., and Lu, H. (2023). Extracellular and intracellular functions of coiled-coil domain containing 3. J. Mol. Cell Biol. *15*, mjad037. https://doi.org/10.1093/jmcb/mjad037.

26. Azad, A., Chakrabarti, S., Xu, Z., Davidge, S., and Fu, Y. (2014). Coiled-coil domain containing 3 (CCDC3) represses tumor necrosis factor-α/nuclear factor κB-induced endothelial inflammation. Cell. Signal. *26*, 2793–2800. https://doi.org/10.1016/j.cellsig.2014.08.025.

27. Kobayashi, S., Kita, S., Okuzaki, D., Fujishima, Y., Otsuki, M., Kato, H., Nishizawa, Y., Miyashita, K., Yokoyama, C., Fukuhara, A., et al. (2022). Favine/CCDC3 deficiency accelerated atherosclerosis and thrombus formation is associated with decreased MEF2C-KLF2 pathway. iScience *25*, 105252. https://doi.org/10.1016/j.isci.2022.105252.

28. Xiao, Q., Li, Y., Cai, B., Huang, X., Fang, L., Liang, F., Chen, L., Xu, K., Zhang, W., Wang, X., et al. (2025). CCDC80 protects against aortic dissection and rupture by maintaining the contractile smooth muscle cell phenotype. Adv. Sci. *12*, 2502108. https://doi.org/10.1002/advs.202502108.

29. Bennett, M.R., Sinha, S., and Owens, G.K. (2016). Vascular smooth muscle cells in atherosclerosis. Circ. Res. *118*, 692–702. https://doi.org/10.1161/CIRCRESAHA.115.306361.

30. Starke, R.M., Chalouhi, N., Ding, D., Raper, D.M., Mckisic, M.S., Owens, G.K., Hasan, D.M., Medel, R., and Dumont, A.S. (2014). Vascular smooth muscle cells in cerebral aneurysm pathogenesis. Transl. Stroke Res *5*, 338–346. https://doi.org/10.1007/s12975-013-0290-1.

31. Hu, Y., Cai, Z., and He, B. (2023). Smooth muscle heterogeneity and plasticity in health and aortic aneurysmal disease. Int. J. Mol. Sci. *24*, 11701. https://doi.org/10.3390/ijms241411701.

32. Pedroza, A.J., Tashima, Y., Shad, R., Cheng, P., Wirka, R., Churovich, S., Nakamura, K., Yokoyama, N., Cui, J.Z., Iosef, C., et al. (2020). Single-cell transcriptomic profiling of vascular smooth muscle cell phenotype modulation in Marfan syndrome aortic aneurysm. Arterioscler. Thromb. Vasc. Biol. *40*, 2195–2211. https://doi.org/10.1161/ATVBAHA.120.314670.

33. Aiuti, A., Webb, I., Bleul, C., Springer, T., and Gutierrez-Ramos, J. (1997). The chemokine SDF-1 is a chemoattractant for human CD34+ hematopoietic progenitor cells and provides a new mechanism to explain the mobilization of CD34+ progenitors to peripheral blood. J. Exp. Med. *185*, 111–120. https://doi.org/10.1084/jem.185.1.111.

34. He, Y.-B., Jin, H.-Z., Zhao, J.-L., Wang, C., Ma, W.-R., Xing, J., Zhang, X.-B., Zhang, Y.-Y., Dai, H.-D., Zhao, N.-S., et al. (2022). Single-cell transcriptomic analysis reveals differential cell subpopulations and distinct phenotype transition in normal and dissected ascending aorta. Mol. Med. *28*, 158. https://doi.org/10.1186/s10020-022-00584-4.

35. Swirski, F.K., and Nahrendorf, M. (2013). Leukocyte behavior in atherosclerosis, myocardial infarction, and heart failure. Science *339*, 161–166. https://doi.org/10.1126/science.1230719.

36. Döring, Y., Drechsler, M., Soehnlein, O., and Weber, C. (2015). Neutrophils in atherosclerosis: from mice to man. Arterioscler. Thromb. Vasc. Biol. *35*, 288–295. https://doi.org/10.1161/ATVBAHA.114.303564.

37. Fernández-Ruiz, I. (2018). NETs are involved in AAA. Nat. Rev. Cardiol. *15*, 257. https://doi.org/10.1038/nrcardio.2018.36.

38. Yang, S., Chen, L., Wang, Z., Chen, J., Ni, Q., Guo, X., Liu, W., Lv, L., and Xue, G. (2023). Neutrophil extracellular traps induce abdominal aortic aneurysm formation by promoting the synthetic and proinflammatory smooth muscle cell phenotype via Hippo-YAP pathway. Transl. Res. *255*, 85–96. https://doi.org/10.1016/j.trsl.2022.11.008.

39. Puchenkova, O., Soldatov, V., Belykh, A., Bushueva, O., Piavchenko, G., Venediktov, A., Shakhpazyan, N., Deykin, A., Korokin, M., and Pokrovskiy, M. (2022). Cytokines in abdominal aortic aneurysm: master regulators with clinical application. Biomark. Insights *17*, 11772719221095676. https://doi.org/10.1177/11772719221095676.

40. Zhao, Y.-F., Zuo, Z.-A., Li, Z.-Y., Yuan, Y., Hong, S.-C., Fu, W.-G., Zhou, B., and Wang, L.-X. (2024). Integrated multi-omics profiling reveals neutrophil extracellular traps potentiate aortic dissection progression. Nat. Commun. *15*, 10736. https://doi.org/10.1038/s41467-024-55038-8.

41. Chen, J., Bai, Y., Xue, K., Li, Z., Zhu, Z., Li, Q., Yu, C., Li, B., Shen, S., Qiao, P., et al. (2023). CREB1-driven CXCR4hi neutrophils promote skin inflammation in mouse models and human patients. Nat. Commun. *14*, 5894. https://doi.org/10.1038/s41467-023-41484-3.

42. Michineau, S., Franck, G., Wagner-Ballon, O., Dai, J., Allaire, E., and Gervais, M. (2014). Chemokine (C-X-C motif) receptor 4 blockade by AMD3100 inhibits experimental abdominal aortic aneurysm expansion through anti-inflammatory effects. Arterioscler. Thromb. Vasc. Biol. *34*, 1747–1755. https://doi.org/10.1161/ATVBAHA.114.303913.

43. Kurilshikov, A., Medina-Gomez, C., Bacigalupe, R., Radjabzadeh, D., Wang, J., Demirkan, A., Le Roy, C., Raygoza Garay, J., Finnicum, C., Liu, X., et al. (2021). Large-scale association analyses identify host factors influencing human gut microbiome composition. Nat. Genet. *53*, 156–165. https://doi.org/10.1038/s41588-020-00763-1.

44. Lopera-Maya, E., Kurilshikov, A., van der Graaf, A., Hu, S., Andreu-Sánchez, S., Chen, L., Vila, A., Gacesa, R., Sinha, T., Collij, V., et al. (2022). Effect of host genetics on the gut microbiome in 7,738 participants of the Dutch Microbiome Project. Nat. Genet. *54*, 143–151. https://doi.org/10.1038/s41588-021-00992-y.

45. Roychowdhury, T., Klarin, D., Levin, M.G., Spin, J.M., Rhee, Y.H., Deng, A., Headley, C.A., Tsao, N.L., Gellatly, C., Zuber, V., et al. (2023). Genome-wide association meta-analysis identifies risk loci for abdominal aortic aneurysm and highlights PCSK9 as a therapeutic target. Nat. Genet. *55*, 1831–1842. https://doi.org/10.1038/s41588-023-01510-y.

46. Võsa, U., Claringbould, A., Westra, H.-J., Bonder, M.J., Deelen, P., Zeng, B., Kirsten, H., Saha, A., Kreuzhuber, R., and Yazar, S. (2021). Large-scale cis- and trans-eQTL analyses identify thousands of genetic loci and polygenic scores that regulate blood gene expression. Nat. Genet. *53*, 1300–1310. https://doi.org/10.1038/s41588-021-00913-z.

47. Zhang, J., Tang, Y., Zhang, S., Xie, Z., Ma, W., Liu, S., Fang, Y., Zheng, S., Huang, C., and Yan, G. (2025). Mitochondrial NAD+ deficiency in vascular smooth muscle impairs collagen III turnover to trigger thoracic and abdominal aortic aneurysm. Nat. Cardiovasc. Res. *4*, 275–292. https://doi.org/10.1038/s44161-025-00607-z.

48. Folkersen, L., Wågsäter, D., Paloschi, V., Jackson, V., Petrini, J., Kurtovic, S., Maleki, S., Eriksson, M.J., Caidahl, K., and Hamsten, A. (2011). Unraveling divergent gene expression profiles in bicuspid and tricuspid aortic valve patients with thoracic aortic dilatation: the ASAP study. Mol. Med. *17*, 1365–1373. https://doi.org/10.2119/molmed.2011.00248.

49. Li, Y., Ren, P., Dawson, A., Vasquez, H.G., Ageedi, W., Zhang, C., Luo, W., Chen, R., Li, Y., Kim, S., et al. (2020). Single-cell transcriptome analysis reveals dynamic cell populations and differential gene expression patterns in control and aneurysmal human aortic tissue. Circulation *142*, 1374–1388. https://doi.org/10.1161/CIRCULATIONAHA.120.046528.

50. Watanabe, K., Taskesen, E., van Bochoven, A., and Posthuma, D. (2017). Functional mapping and annotation of genetic associations with FUMA. Nat. Commun. *8*, 1826. https://doi.org/10.1038/s41467-017-01261-5.

51. Papayannopoulos, V. (2018). Neutrophil extracellular traps in immunity and disease. Nat. Rev. Immunol. *18*, 134–147. https://doi.org/10.1038/nri.2017.105.

52. Zhang, Y., Guo, L., Dai, Q., Shang, B., Xiao, T., Di, X., Zhang, K., Feng, L., Shou, J., and Wang, Y. (2022). A signature for pan-cancer prognosis based on neutrophil extracellular traps. J. Immunother. Cancer *10*, e004210. https://doi.org/10.1136/jitc-2021-004210.

STAR★METHODS

KEY RESOURCES TABLE

REAGENT or RESOURCE	SOURCE	IDENTIFIER
Antibodies		
Rabbit polyclonal anti-CCDC3	Affinity Biosciences	Cat# DF16031
Rabbit polyclonal anti-CXCL12	Proteintech	Cat# 17402-1-AP; RRID:AB_2878404
Rabbit polyclonal anti-TAGLN/SM22α	Abcam	Cat# ab14106; RRID:AB_443021
Rabbit polyclonal anti-MMP2	Abcam	Cat# ab97779; RRID:AB_10696122
Rabbit polyclonal anti-ACTA2 (α-SMA)	Abcam	Cat# ab5694; RRID:AB_2223021
Mouse monoclonal anti-CXCR4	Proteintech	Cat# 60042-1-Ig; RRID:AB_2091809
Rabbit polyclonal anti-S100A8	Proteintech	Cat# 15792-1-AP; RRID:AB_10666315
Rabbit polyclonal anti-CitH3 (citrullinated histone H3)	Abcam	Cat# ab5103; RRID:AB_304752
Rabbit polyclonal anti-β-tubulin	Abcam	Cat# ab6046; RRID:AB_2210370
Chemicals, peptides, and recombinant proteins		
Angiotensin II (Ang II)	MedChemExpress	Cat# HY-13948
Lipofectamine RNAiMAX Transfection Reagent	Thermo Fisher Scientific	Cat# 13778150
Opti-MEM I Reduced-Serum Medium	Thermo Fisher Scientific	Cat# 31985062
SmBM Smooth Muscle Cell Basal Medium	Lonza	Cat# CC-3181
SmBM BulletKit supplements	Lonza	Cat# CC-4149
Critical commercial assays		
Human CXCL12/SDF-1α Quantikine ELISA Kit	R&D Systems	Cat# DSA00
Deposited data		
scRNA-seq	GEO	GSE155468
Bulk RNA-seq	GEO	GSE235161
Microarray	GEO	GSE26155
Spatial transcriptome	China National Center for Bioinformatics	HRA004063
Aortic aneurysm	AAAGen	https://csg.sph.umich.edu/willer/public/AAAgen2023/
Aortic aneurysm	Pan-UKBB	https://pan.ukbb.broadinstitute.org/
Gut microbiota taxa	MiBioGen	https://doi.org/10.1038/s41588-020-00763-1
Gut microbiota taxa and pathways	Dutch Microbiome Project	https://doi.org/10.1038/s41588-021-00992-year
Plasma eQTL	eQTLGEN	https://www.eqtlgen.org/cis-eqtls.html
Experimental models: Cell lines		
Human Aortic Smooth Muscle Cells (HASMCs)	Lonza	Cat# CC-2571
Oligonucleotides		
Non-targeting scramble siRNA (negative control)	Ambion/Thermo Fisher Scientific	Cat# 4390846
CCDC3-specific siRNA	Ambion/Thermo Fisher Scientific	Cat# 4457298
Software and algorithms		
Monocle 3 (trajectory analysis)	Github	https://cole-trapnell-lab.github.io/monocle3/

(*Continued on next page*)

Continued

REAGENT or RESOURCE	SOURCE	IDENTIFIER
WGCNA (weighted gene co-expression network analysis)	Github	https://horvath.genetics.ucla.edu/html/CoexpressionNetwork/Rpackages/WGCNA/
CellChat (cell-cell communication)	Github	https://github.com/sqjin/CellChat
NicheNet (ligand-receptor interaction)	Github	https://github.com/saeyslab/nichenetr
Scissor (phenotype-associated cell identification)	Github	https://github.com/sunduanchen/Scissor
CIBERSORTx (bulk RNA-seq deconvolution)	Github	https://cibersortx.stanford.edu/
pySCENIC (transcription factor regulon inference)	Github	https://github.com/aertslab/pySCENIC
decoupleR/AUCell (pathway activity scoring)	Github	https://github.com/saezlab/decoupleR
BayesSpace (spatial transcriptomics super-resolution)	Github	https://github.com/edward130603/BayesSpace
FUMA (functional mapping and annotation of GWAS)	FUMA	https://fuma.ctglab.nl/
CMap cloud platform (drug connectivity mapping)	Broad Institute	https://clue.io/
ImageJ	NIH	https://imagej.nih.gov/ij/

EXPERIMENTAL MODEL AND STUDY PARTICIPANT DETAILS

Human aortic tissue samples

The study protocol adhered to the Declaration of Helsinki and was approved by the Clinical Research Ethics Committee of Tianjin Medical University General Hospital (IRB2026-YX-084-01). Human aortic tissue specimens were obtained from four patients who underwent open surgery. Aneurysmal tissues (n = 4) were collected from the dilated aneurysmal sac. Non-aneurysmal tissues (n = 4) were collected from the non-dilated neck. All patients provided written informed consent. Demographic details, including gender, age, and ethnicity, are presented in Table S1. Sex-specific analyses were not conducted, as the study was not powered to detect sex-based differences.

Cell culture

Human aortic smooth muscle cells (HASMCs; CC-2571, Lonza) were cultured in SmBM medium supplemented with the SmBM BulletKit (CC-3181 and CC-4149, Lonza) and maintained at 37°C in a humidified atmosphere containing 5% CO_2. Cell authenticity was validated by the robust expression of VSMC-specific markers. The cells were routinely monitored and verified as mycoplasma-negative.

METHOD DETAILS

Cell treatment and transfection

For gene silencing, cells (passages 3–5) were serum-starved in Opti-MEMI Reduced-Serum Medium (Thermo Fisher Scientific) for 4 h, then transfected with either non-targeting scramble siRNA (4390846, Ambion) or CCDC3-specific siRNA (4457298, Ambion) at a final concentration of 10 nM using Lipofectamine RNAiMAX (Thermo Fisher Scientific).To model VSMC phenotypic remodeling, cells were stimulated with angiotensin II (Ang II;1 μM, HY-13948, MedChemExpress) for 48 h.

Western blotting

HASMCs were lysed using SDS-PAGE loading buffer. Equal amounts of protein were resolved on 10% SDS-PAGE gels and transferred onto PVDF membranes. The membranes were blocked with 5% BSA for 1 h, followed by overnight incubation at 4°C with the following primary antibodies: β-tubulin (Abcam, ab6046), CCDC3 (Affinity Biosciences, DF16031), CXCL12 (Proteintech, 17402-1-AP), TAGLN/SM22α (Abcam, ab14106), and MMP2 (Abcam, ab97779). After a 1 h incubation with secondary antibodies at room temperature, the protein bands were visualized using an enhanced chemiluminescence kit. Band intensities were subsequently quantified by densitometric analysis using ImageJ software.

ELISA

The cell culture supernatant was collected from different treatment groups to determine the CXCL12 level using an ELISA kit (DSA00, R&D Systems). All the procedures were carried out according to the manufacturer's instructions.

Histological and immunofluorescence staining

We performed overnight immersion-fixation of aortic samples in 4% paraformaldehyde, followed by paraffin embedding after dehydration through increasing ethanol concentrations. To assess elastic fiber integrity, we utilized Verhoeff-van Gieson (VVG) staining according to established procedures (Figure S9). Elastin destruction level was quantified according to the grading system: Grade I (0–25%), Grade II (26–50%), Grade III (51–75%), and Grade IV (76–100%). The tyramide signal amplification (TSA) method was employed to enhance the fluorescence signaling. After cell permeabilization, sections were stained with primary antibodies against ACTA2 (Abcam), CCDC3 (Affinity), CXCL12, S100A8, CXCR4 (Proteintech), and CitH3 (Abcam), with DAPI used for nuclear visualization.

Data sources

The MiBioGen consortium provided SNPs linked to 211 microbial taxa, ranging from the phylum to genus level, incorporating data from 25 cohorts with a collective of 18,340 participants.[43] Dutch Microbiome Project provided genetic data for microbial species, containing 7,738 individuals from European ancestry.[44] Additionally, the discovery cohort was acquired from a meta-analysis of GWAS, encompassing 17 cohorts with 392,11 AA patients and 1,086,107 controls.[45] UK Biobank was used for validation, including 1,306 AA patients and 408,565 controls (Table S1). The eQTLGen consortium contributed gene expression quantitative trait loci (eQTL) data from 31,684 European populations.[46] We collected human aortic transcriptome data available in the Gene Expression Omnibus (GEO, https://www.ncbi.nlm.nih.gov/geo/). The bulk RNA-sequencing (RNA-seq) dataset (GSE235161)[47] and microarray dataset (GSE26155)[48] were collected for deconvolution analysis. Single-cell RNA-sequencing (scRNA-seq) dataset (GSE155468)[49] included aortic wall tissue from 8 AA patients and 3 healthy donors.

MR design

MR analysis was performed to estimate the causality between gut microbiota and AA (Figure S1). Instrumental variants selection was based on the following criteria: (1) SNPs associated with gut microbiota taxa using a relaxed threshold ($p < 1 \times 10^{-5}$); (2) Independent SNPs were retained after the computation of linkage disequilibrium among pertinent SNPs with threshold $r^2 = 0.001$ and distance >10,000 kb; (3) The value of F-statistic >10 was regarded as indicative of substantial statistical power. The inverse variance weighted (IVW) method serves as the main tool to estimate effects. To ensure the robustness of the MR findings, complementary analyses were performed using MR Egger, weighted mode, and weighted median. MR pleiotropy residual sum and outlier (MR-PRESSO) global test and MR-Egger regression were designed to quantify horizontal pleiotropy. Cochran's Q Test was implemented to assess heterogeneity. The stability of estimates was further examined through leave-one-out analysis. The top *cis*-QTL was utilized to examine the causality between host gene expression and AA using summary-level MR (SMR), which was selected within a ±1000 kb window around the target gene with a threshold of $p < 5 \times 10^{-8}$. To distinguish pleiotropy effects and linkage disequilibrium in the associations, the Heterogeneity in Dependent Instruments (HEIDI) test was applied. Associations were considered potentially pleiotropic and excluded if the HEIDI test was less than 0.01. MR analysis was further employed to examine the robustness of SMR results.

Genetic annotation and tissue enrichment

To further investigate the gene-microbiota association, we utilized FUMA analysis (https://fuma.ctglab.nl/) to annotate lead SNPs to genes based on their positions.[50] Furthermore, we assessed the pan-tissue expression specificity of protein-coding mapped genes in the Genotype-Tissue Expression Portal (GTEx v8) atlas.

Single-cell transcriptomics analysis

For dimensionality reduction and clustering, the top 2,000 variable genes were selected using the FindVariableFeatures function. The Harmony algorithm was applied to mitigate batch effects across different samples. A nearest-neighbor graph was constructed based on the top 20 principal components using the FindNeighbors function. Cell clusters were identified using the FindClusters function and visualized via Uniform Manifold Approximation and Projection (UMAP). Differential gene expression between AA and normal tissues was assessed using the Wilcoxon rank-sum test with Benjamini-Hochberg adjustment. Weighted gene co-expression network analysis (WGCNA) was employed to construct co-expression networks and identify highly co-expressed gene modules. The Scissor algorithm was employed to identify disease-relevant cell subsets via integrating phenotypic information from the RNA-seq dataset.[12] Scissor constructed a similarity network and quantified the correspondence between scRNA-seq and RNA-seq using Pearson correlation coefficients. VSMCs were categorized into Scissor+ (positive correlation) or Scissor- (negative correlation) subpopulations.

Deconvolution analysis for RNA-seq

To estimate the proportion of cell subsets from bulk transcriptomic datasets, we applied the CIBERSORTx deconvolution algorithm. A reference signature matrix was constructed from the scRNA-seq dataset to infer cell subset composition in bulk RNA-seq and microarray data. For RNA-seq data, quartile normalization was disabled, whereas for microarray data, it was enabled. The imputation

step was conducted with 500 permutations. Subsequently, pairwise correlations among the inferred cell-type fractions were evaluated using Spearman's correlation analysis.

Functional pathway and gene set enrichment analysis

Gene Ontology (GO) and Kyoto Encyclopedia of Genes and Genomes (KEGG) pathway enrichment analysis were performed using the ClusterProfiler package. Pathway signaling activities were calculated with the AUCell function from the decoupleR package. The NETs activity in the scRNA-seq and bulk RNA-seq datasets was evaluated using the AUCell and ssGSEA packages, respectively. The NETs-related gene set was provided in Table S2.[51,52] The pySCENIC method was employed to infer transcription factors and quantify regulon activity in distinct cell subsets.

Trajectory analysis

To investigate the differentiation trajectories of VSMC subtypes, we employed the Monocle 3 algorithm. Dimensionality reduction was performed using the UMAP method. Subsequently, the trajectory timeline was inferred by the learn_graph function. In addition, the branch expression analysis was employed to elucidate the dynamics of gene expression along branching trajectories.

Cell-cell communications analysis

To systematically uncover cell communication networks in the aortic microenvironment, we applied the CellChat package. This approach leverages a repository of ligand-receptor interactions to infer cell communication probability. Significant interactions were defined by the co-expression of ligand-receptor pairs among distinct cell populations. To specifically investigate cell signaling between VSMCs and neutrophils, we further applied the NicheNet algorithm. This method integrates expression data with prior signaling knowledge to quantitatively predict ligand-mediated gene regulatory effects. The top 10 predicted ligands originating from VSMCs and their regulatory influence on the top 100 target genes in myeloid cells were prioritized.

Spatial transcriptomics analysis

To enhance the spatial resolution of gene expression features, spatial spots were enhanced using the BayesSpace package. Cell-type signature scores derived from the scRNA-seq reference dataset were projected onto the spatial transcriptomic dataset by computing module scores via the AddModuleScore function in Seurat, with all parameters set to default, and the resulting scores were appended to the Seurat object metadata for correlation analysis.

Drug sensitivity analysis

The Connectivity Map (CMap) serves as a valuable resource to identify potential therapeutic small-molecule drugs. We employed the query tool in the cloud-based CMap platform to perform drug prediction, mode of action analysis, and drug-target evaluation. The connectivity score was calculated by comparing the input gene set against the reference profiles in the database. According to the pattern-matching algorithm, a positive connectivity score reflects the induction of the query signature by a small molecule, whereas a negative score indicates suppression.

QUANTIFICATION AND STATISTICAL ANALYSIS

Data are presented as the mean ± standard deviation. Normality was assessed using the Shapiro-Wilk test. For normally distributed data, the *t* test or one-way ANOVA followed by Tukey's post-hoc test was employed for group comparisons. For non-normally distributed data, the Mann-Whitney U test or the Kruskal-Wallis test was applied. The "n" values reported in the figure legends represent independent biological replicates. All statistical analyses were performed using GraphPad Prism (version 9.0.1), and $p < 0.05$ was considered statistically significant.